Spin-Polarized Scanning Tunneling Microscopy of Magnetic Structures and Antiferromagnetic Thin Films

Wulf Wulfhekel[1] and Jürgen Kirschner[2]

[1]Physikalisches Institut, Universität Karlsruhe (TH), 76131 Karlsruhe, Germany; email: wulf.wulfhekel@pi.uni-karlsruhe.de

[2]Max-Planck Institut für Mikrostrukturphysik, 06120 Halle, Germany

Annu. Rev. Mater. Res. 2007. 37:69–91

First published online as a Review in Advance on February 8, 2007

The *Annual Review of Materials Research* is online at http://matsci.annualreviews.org

This article's doi: 10.1146/annurev.matsci.37.052506.084342

1531-7331/07/0804-0069$20.00

Key Words

magnetic imaging, magnetic nanostructures, antiferromagnets, spin polarization, spin structure

Abstract

We present an overview of the technique of spin-polarized scanning tunneling microscopy (Sp-STM) and its application to high-resolution magnetic imaging. In STM, the electron density near the sample surface is imaged. Additionally, Sp-STM allows a mapping of the spin polarization of the electronic density, which is related to the magnetic configuration of the sample. Two primary imaging modes of Sp-STM are currently in use: the spectroscopic mode and the differential magnetic mode. The principles of the two modes are explained in the framework of imaging ferromagnetic nanostructures and antiferromagnetic surfaces. The advantages and drawbacks of the two approaches are discussed, and the strength of Sp-STM to map even complex spin structures on the nanometer scale is illustrated.

INTRODUCTION

MRAM: magnetic random-access memory

Magnetic anisotropy: variation of the energy density of a ferromagnetic crystal upon changes in the orientation of magnetization. It is caused by the spin-orbit interaction

Spin polarization: difference of the density of states of majority and minority electrons divided by their sum

Sp-STM: spin-polarized scanning tunneling microscopy

Tunneling: the quantum mechanical transport of electrons through a potential barrier, which is forbidden in classical physics

STM: scanning tunneling microscopy

Density of states: density of available states of the electrons in the solid. Below the Fermi energy, states are occupied, and above they are unoccupied

The magnetic properties of nanoscale magnets have been the focus of intensive research in the past few decades. On the one hand, the study of magnetism on the nanoscale has been a driving force for the revolutionary development of high-density magnetic storage devices, magnetic random-access memory (MRAM), and magnetic sensors (1–4). On the other hand, many fundamental issues regarding the physics of magnetism and antiferromagnetism are related to nanoscale properties. Questions about the magnetic anisotropy, magnetic ordering temperature, spin polarization, coercive fields and exchange bias, and micromagnetic configuration have been related to properties on the atomic scale (5–7). Although these aspects led to a convergence of experimental magnetism and ab initio theory (8), a local imaging technique to map magnetic properties in real space on the atomic level had been lacking until the development of spin-polarized scanning tunneling microscopy (Sp-STM). This real-space imaging technique enables one to explore magnetic structure down to the atomic level, to verify the theoretical predictions, and to place many phenomenological models on a solid microscopic base.

In scanning tunneling microscopy (STM), the electrons that tunnel between the tip and a conductive surface are used as a feedback parameter to position the tip. During scanning along lines in the constant current mode, the apex of the tip is held on equicurrent lines several Ångstroms above the sample surface by the feedback mechanism. In the well-established Tersoff-Hamann model (9, 10), the constant current scan lines correspond to the lines of constant charge density of the sample surface. A plot of the z-coordinate, i.e., the vertical tip position regulated by the feedback as a function of the lateral position x and y, is therefore termed a topographic STM image and reflects the spatial distribution of the density of states of the electrons (11). In case of a sharp tip apex, individual atoms can be resolved in topographic images (12).

The above picture neglects the spin of the electron. For paramagnetic substances, this simplification is justified, as the electron density does not depend on the spin. For ferromagnetic or antiferromagnetic materials, however, the density of states is spin-split into majority and minority states, and a net imbalance between the occupation of both leads to the development of a magnetic moment in the atoms. In Sp-STM the tip itself is spin polarized. Information on the spin polarization of the sample surface may be obtained via the spin-dependent tunneling process between tip and sample. If the spin-dependent part of the tunneling current can be separated, it is possible to obtain information on the magnetic configuration of a sample surface with the same lateral resolution as for topographic information, i.e., with atomic resolution. Thus, Sp-STM is the magnetic imaging technique with the ultimate lateral resolution, which is suitable for probing magnetism in nanostructures or even the magnetic configuration of antiferromagnets in real space. There are various approaches with which to separate the spin-dependent part from the spin-independent part of the tunneling current; the following section discusses two of these. After introducing in detail the principles of spin-polarized tunneling, we give examples for imaging both ferromagnetic and antiferromagnetic surfaces.

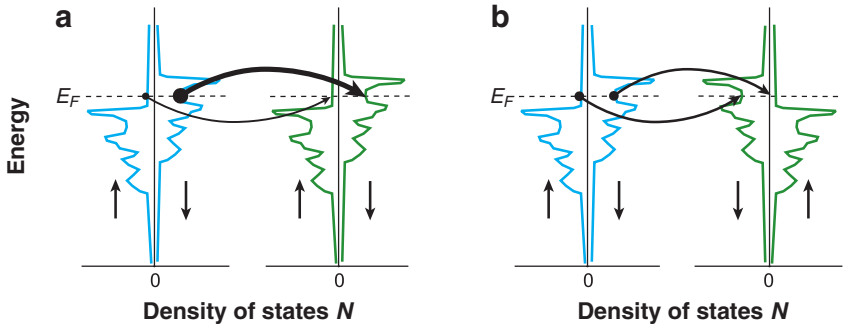

Figure 1

Tunneling between two ferromagnetic electrodes that show a spin-split density of states N (↑ and ↓ indicate majority and minority states, respectively). In *a* the magnetization of the two electrodes is parallel, whereas it is antiparallel in *b*. The conductivities for tunneling from the left to the right electrode are indicated by arrows.

Spin-Polarized Tunneling

The principle of operation of Sp-STM is based on the fundamental property of ferromagnets and antiferromagnets, i.e., that their magnetic moment is related to an imbalance in occupation of electrons of different spins. Owing to the quantum mechanical exchange interaction between electrons, the density of states splits up into minority and majority states, as shown in **Figure 1*a***. The imbalance causes a spin polarization, in contrast to paramagnetic substances, in which the distributions of spin-up and spin-down electrons are identical. The splitting of the density of states has immediate consequences on the tunneling current, as Jullière (13) discovered. When electrons tunnel between two ferromagnets, the magnitude of the current is influenced by the magnetization of the two electrodes. The phenomenon was therefore referred to as the tunneling magnetoresistance (TMR) effect. In a magnetic tunneling junction, two magnetic electrodes are separated by a thin insulator. The tunneling conductance G depends on the relative orientation of the magnetization of the two electrodes. For parallel orientation, G usually is higher than for antiparallel orientation. This finding can be explained on the basis of a simple model for tunneling in which we neglect any spin dependence in the transmission through the barrier and focus solely on the electronic properties of the two electrodes. Under the assumption of a small bias voltage across the junction and in the absence of spin-flip scattering during the tunneling process, the electrons in the ferromagnets near the Fermi energy determine the tunneling conductance of the junction. For the parallel orientation, the majority/minority electrons of the first electrode tunnel into the majority/minority states, respectively, in the second electrode, as shown in **Figure 1*a***. Per Fermi's golden rule, the conductance G is proportional to the density N of initial (i) and final (f) states at the Fermi edge. Upon the combination of both spin channels, the conductance for parallel-oriented magnetizations is given by

$$G_{\uparrow\uparrow} \propto N_{\uparrow}^{i} N_{\uparrow}^{f} + N_{\downarrow}^{i} N_{\downarrow}^{f}. \qquad 1.$$

Exchange interaction: quantum mechanical coupling between two spins. For ferromagnetic substances, a parallel alignment of spins is favored

TMR: tunneling magnetoresistance

Sp-STS: spin-polarized scanning tunneling spectroscopy

For the antiparallel orientation, electrons of majority character in one electrode tunnel into states of minority character in the other electrode (cf. **Figure 1*b***), and the conductance is given by the mixed products

$$G_{\uparrow\downarrow} \propto N_{\uparrow}^{i} N_{\downarrow}^{f} + N_{\downarrow}^{i} N_{\uparrow}^{f}. \qquad 2.$$

These two conductivities generally are not identical, leading to a variation of the tunneling current with the magnetic configuration of the electrodes. Slonczewski (14) treated the problem of spin-polarized tunneling more rigorously. Neglecting higher-order spin effects, he calculated the dependence of G on the angle θ between the magnetization of the two electrodes. With the spin polarization $P = (N_{\uparrow} - N_{\downarrow})/(N_{\uparrow} + N_{\downarrow})$, the conductance is given by

$$G = G_0(1 + P^i P^f \cos\theta). \qquad 3.$$

Slonczewski's prediction for the angular dependence of the TMR effect was later experimentally confirmed (15).

If a finite bias is applied, all states between the two Fermi levels are involved in tunneling. They have to be weighted according to their tunneling probability through the barrier, which may depend on the energy or other parameters. This scenario is more complex, but G can be expressed using effective, i.e., correctly weighted, densities or polarizations.

THE TWO IMAGING MODES

In a conventional STM experiment, the tunneling current is used to extract information regarding the electronic density. In Sp-STM the TMR effect is used to obtain magnetic information from the tunneling current. Instead of a nonmagnetic tip, a spin-polarized tip (magnetic or antiferromagnetic) is used to map the magnetic surface. Therefore, one needs a method to separate magnetic and nonmagnetic information in the tunneling current to image topographic and magnetic properties of the sample surface separately. There have been several modes proposed to achieve this (16). Some of them only partly separate the spin information from the topography (17), and some modes have not been of large success (18). In the following subsections, we restrict ourselves to discussing the two most important modes: the spectroscopic mode and the differential magnetic mode.

The Spectroscopic Mode

Under certain circumstances, the spectroscopic mode of Sp-STM allows one to separate topographic and spin information. This mode is also named spin-polarized scanning tunneling spectroscopy (Sp-STS). Although Pierce (16) proposed this mode in 1988, Bode et al. (19) first realized it ten years later. It uses the energy dependence of the spin polarization of the sample density of states. To illustrate the mode of operation, let us assume that the spin polarization of the tip does not depend on the energy, in accord with the Tersoff-Hamann model of STM. When the magnetic surface is imaged in the constant current mode, any variations of the conductance G

due to the TMR effect according to Equation 3 are compensated by changes in the tip sample distance. As a result, the topographic image contains information both on the electronic density and on the spin. In Sp-STS, the feedback loop of the STM is then switched off, and U is varied, e.g., it is increased. As a consequence, the tunneling current changes. If the spin polarization of the sample increases with energy, the tunneling current for a parallel-oriented tip and sample magnetization increases more than for an antiparallel orientation, following Equation 3. Pierce (16) suggested that U can be varied significantly. Nevertheless, the imaging mode also works for low modulation of U. In this case, the variations in the tunneling current are proportional to the differential conductance dI/dU. In the pioneering experiment by Bode et al. (19), the observed peak height of the spin-split surface state of Gd(0001) in laterally resolved dI/dU spectra was used to obtain magnetic information. The imaging mode is now widely used. Tips coated with a thin film of a ferromagnet or antiferromagnet are used as spin-polarized tips. This way, the magnetic stray field of the tips can be minimized or completely avoided (20, 21). The disadvantage of this mode is that the dI/dU signal in Sp-STS only weakly depends on magnetism. It depends much more strongly on general variations of the density of states caused by, e.g., compositional, structural, or morphological inhomogeneities of the sample. This limits the use of this approach to surfaces with a homogeneous electronic density of states.

Surface state: electronic state that is confined to the surface of a crystal

The Differential Magnetic Mode

The differential magnetic imaging mode involves the use of a bulk ferromagnetic tip whose magnetization is modulated. Owing to the TMR effect, these modulations lead to modulations of the tunneling current that are related to the spin polarization of the sample. This mode's basic concept is directly related to Equation 3. In this mode, a magnetically bistable tip is used. The tip magnetization is periodically switched between the two stable configurations of opposite magnetization. This is equivalent to changing the sign of the spin polarization of the tip. In the experimental setup, the magnetization of the tip is reversed by an alternating current through a small coil that is fixed to the tip. The frequency of the alternating current lies above the cut-off frequency of the feedback loop of the STM (22). Thus, the feedback loop detects only the averaged tunneling current for the two spin polarizations (positive and negative) of the tip apex. As Equation 3 shows, in the time-averaged tunneling current $\bar{I} = I_0$, all spin-dependent currents cancel out such that that the constant current image contains no magnetic information. With a phase-sensitive lock-in amplifier, the alternating part of the tunneling current ΔI, which is proportional to $P^i P^f \cos\Theta$, is detected. This signal contains all the spin information. This way, topographic and spin information is strictly separated, and an image of the spin component along the magnetization axis of the tip can be recorded simultaneously with the topography (22). Magnetostriction of the tip during the reversal must be avoided in all cases. The early experiments of Johnson et al. (23) suffered from significant magnetostriction of the Ni tip so that no stable magnetic or topographic imaging was possible. The use of magnetostriction-free CoFeSiB tips finally allowed for magnetic imaging in the differential magnetic mode (22, 24). Depending on the shape of the STM tip, the

magnetization direction and therefore the direction of spin sensitivity can be chosen. The use of a sharp and pointed tip allows the out-of-plane component of the spin polarization to be imaged (22). The use of a ring-shaped electrode, in which the magnetization lies tangential to the outer perimeter, allows the in-plane component of the spin polarization to be measured (24). Although these ring-shaped STM electrodes are not sharp on the mesoscopic scale, atomic resolution may be obtained on flat surfaces. The advantage of the differential magnetic mode is that, even when the electronic structure of the sample is arbitrary or varying, the spin polarization can still be measured. The disadvantage of this mode is that no magnetic fields can be applied to the sample during imaging, as this field would prevent the magnetic switching of the tip.

Magnetic domain: region of homogeneous magnetization

ML: monolayers

MAGNETIC NANOSTRUCTURES

Magnetic nanostructures are widely used in magnetic data storage, magnetic sensors, and possibly in future spintronic devices. For data storage, the information must be stored in an unambiguous way. To obtain reliable read-write processes, the particle should be a magnetically bistable system. Highest densities and best signals are obtained on single-domain particles. Therefore, the question of the single-domain limit in information storage is of practical importance. The formation of magnetic domains is often technologically undesirable. In soft magnetic nanostructures, many different states have been proposed, depending on the particle's shape and size (25). The different magnetic states originate from a competition between the magnetic stray field outside the particle and the exchange interaction within the particle. In small particles, the exchange interaction dominates, and the structure is single domain. In contrast, in larger particles, the tendency to reduce the stray field dominates, and magnetic closure patterns are formed. Although the phase diagram of magnetic states in nanostructures of various shapes has been studied from the theoretical approach, direct imaging of the single-domain limit has not been possible owing to the insufficient lateral resolution of magnetic imaging techniques. Similarly, elucidation of the fine structure of magnetization singularities and vortices, which are present in many flux closure configurations, has been out of reach of magnetic imaging techniques. Finally, structural defects also may influence the magnetic configuration on a local scale. Sp-STM is particularly useful in relating structure and magnetism on the atomic scale. Below we give several examples to illustrate the achievements of Sp-STM in magnetic nanostructures.

The Single-Domain Limit

Sp-STM, with its potentially atomic lateral resolution, offers the resolution necessary to determine the single-domain limit experimentally. Experiments were performed in ultrahigh vacuum with a cryogenic STM. W tips were coated with 10 monolayers (ML) of Fe to obtain in-plane spin contrast in the spectroscopic mode (26). The magnetic nanostructures were prepared by deposition of 4.7–6.5 ML of Fe on W(001), followed by annealing to 800 K. This resulted in the self-organized formation of

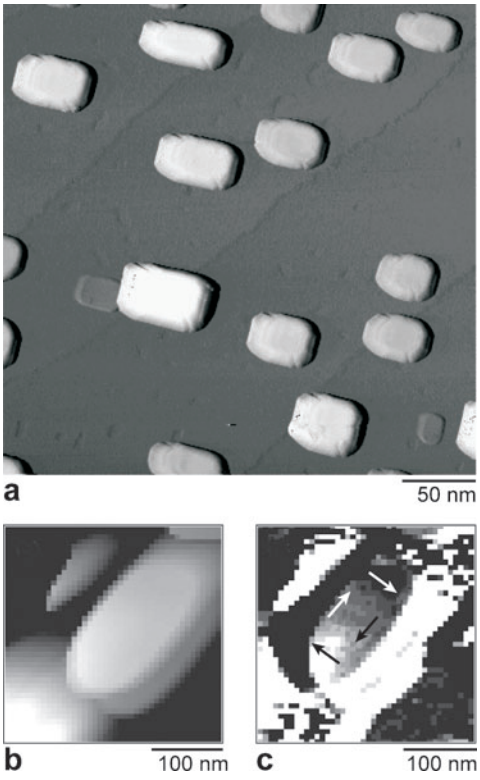

Figure 2

(*a*) Fe nanoislands on W(100). Several Fe islands with a size and thickness of approximately 50 nm and 8 nm, respectively, can be seen. Topography (*b*) and magnetic *dI/dU* image (*c*) of one island. The contrast in *c* reflects a magnetic vortex state. The arrows represent the orientations of magnetization in each area of the vortex.

magnetic nanostructures (27). Magnetic contrast was obtained by recording the differential conductance *dI/dU* close to the minority surface state of Fe(001) at 200 mV above the Fermi energy, as suggested by Stroscio et al. (28). The peak height of the surface state in *dI/dU* spectra recorded with Fe-coated tips was used to obtain the relative orientation between tip and sample magnetization. For parallel magnetization of tip and sample, the peak in the *dI/dU* spectrum is maximal, whereas for antiparallel magnetization, it is minimal.

Figure 2*a* shows a topographic image of self-organized Fe islands. The islands are thick enough that an electronic structure identical to bulk Fe(100) results. This ensures a homogeneous electronic structure within the islands. The size of the Fe island can be controlled by changing the amount of deposited Fe and by varying the annealing temperature. **Figures 2*b*** and ***c*** show the topographic and magnetic *dI/dU* images of an elliptical Fe island on W(001) measured with an Fe-coated tip. The island has an atomically flat top. The contrast in the *dI/dU* image reflects the in-plane magnetization of the sample showing a vortex state with bright, dark, and intermediate areas. The arrows represent the orientations of magnetization in each area of the vortex. For larger islands of similar thickness, flux closure states were always found, and a single-domain state was never observed, indicating that the vortex state is the ground state. Smaller islands, like those displayed in **Figure 3**, never showed

Figure 3

Magnetic *dI/dU* images of two nanoislands below the single-domain limit.

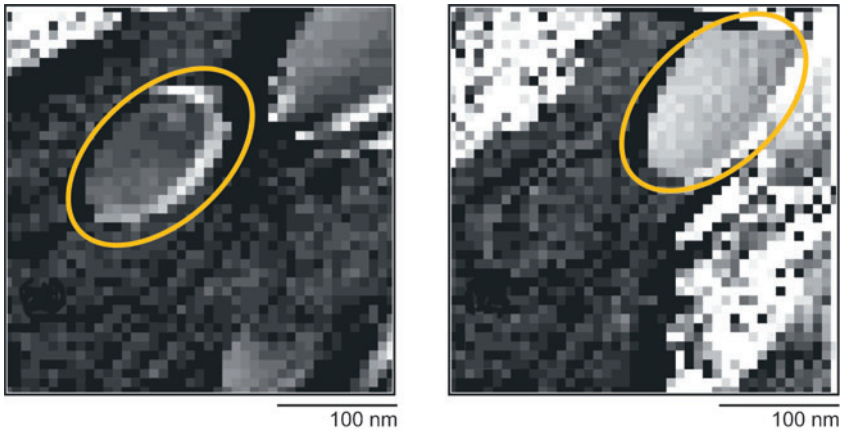

a vortex state but rather always showed a homogeneous contrast. This is consistent with single-domain islands.

From the magnetization pattern of many islands observed with Sp-STM, the experimental magnetic phase diagram shown in **Figure 4** was obtained (29). The single-domain state was always found below a thickness of 6 nm and an average diameter of 120 nm. Analytical and numerical calculations by Cowburn et al. (30) reproduce well the directly observed boundary between the single-domain and vortex states.

Figure 4

Experimental magnetic phase diagram (*dots*) compared with an analytical model (*line*).

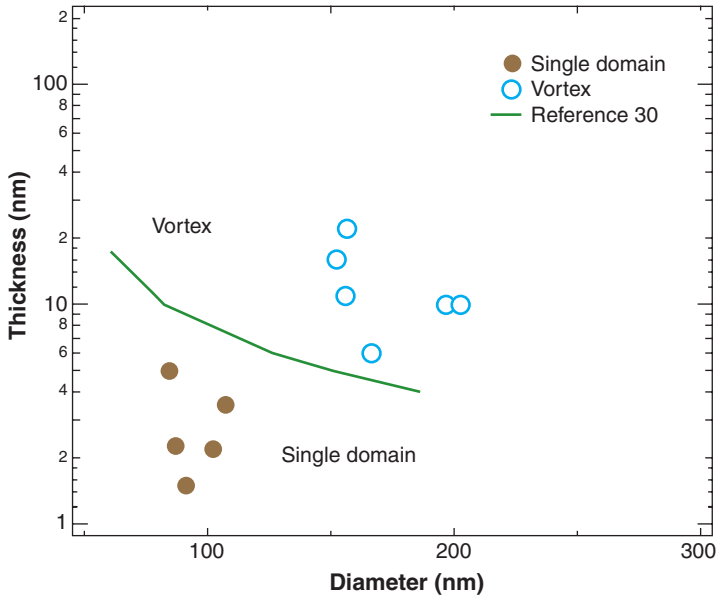

The Structure of Vortex Cores

Vortices play a central role in flux closure patterns of magnetic nanostructures. In a disk-shaped magnet, the stray field is minimized when the magnetization lies tangential to the circumference in the plane of the disk. As the magnetization is a continuous vector field of the constant length of the saturation magnetization ($|\vec{M}| = M_s$), a vortex poses a topological problem in its center. The solution is that the magnetization turns out of the plane in the center of the vortex, as has been observed, e.g., with magnetic force microscopy (31). In the vortex core, the dipolar stray field is increased. It is in competition with the exchange interaction such that the core diameter w_d is given by $w_d = 2\sqrt{2A/\mu_0 M_s^2}$, which is below 10 nm in the case of Fe. Although this configuration was described in detail in micromagnetic models (32), the limited lateral resolution of magnetic imaging techniques did not allow for the resolution of the inner vortex structure. Moreover, Sp-STM using magnetic tips is not suited for resolving the vortex core, as the small stray field of the magnetic tip moves the extremely mobile vortex core such that it only appears blurred, as in **Figure 2*c***. A solution to the magnetostatic interaction problem between tip and sample is to use a tip that shows a spin polarization but no net magnetic moment. This can be achieved in the spectroscopic mode by replacing the ferromagnetic tip with an antiferromagnetic tip. Although the latter shows no net magnetic moment and therefore no magnetic stray field, the last atom of the tip carrying the tunneling current may be spin polarized. A magnetic contrast was obtained with Cr- and Mn-coated tips without influencing the sample magnetization (20, 21).

Cr layers often show an out-of-plane sensitivity. **Figure 5** shows a vortex in more detail. Whereas the in-plane magnetic signal of **Figure 5*b*** shows the circular arrangement of magnetic moments, the core of the vortex is magnetized out of plane, as revealed in **Figure 5*c*** as a black area. Through the use of antiferromagnetic tips, the core of the vortex was resolved (33). The observed line profiles (cf. **Figure 5*d***) agree well with those of micromagnetic calculations. The agreement shows that micromagnetic continuum theory reliably works even down to the range below 10 nm.

Atomic Steps as Pinning Centers for Domain Walls

Magnetization processes in low-dimensional magnetic systems like thin films, wires, and dots play a key role in magnetic recording and future spintronic devices like the MRAM. Magnetization reversal may involve nucleation and propagation of domain walls. Defects in thin films and nanostructures can pin the domain walls, and magnetic reversal may be impeded, affecting device performance. An understanding of the influence of defects [step edges of the substrate (34), constrictions in the magnetic nanostructures (35), etc.] is therefore of high interest and importance. Recent studies have shown that a high density of substrate step edges can lead to anisotropic domain wall propagation in thin magnetic films (34). Sp-STM, with its nanometer resolution in topography and spin, is especially suited for studying magnetic phenomena related to atomic defects. Free walls and walls pinned at atomic substrate steps can be compared directly.

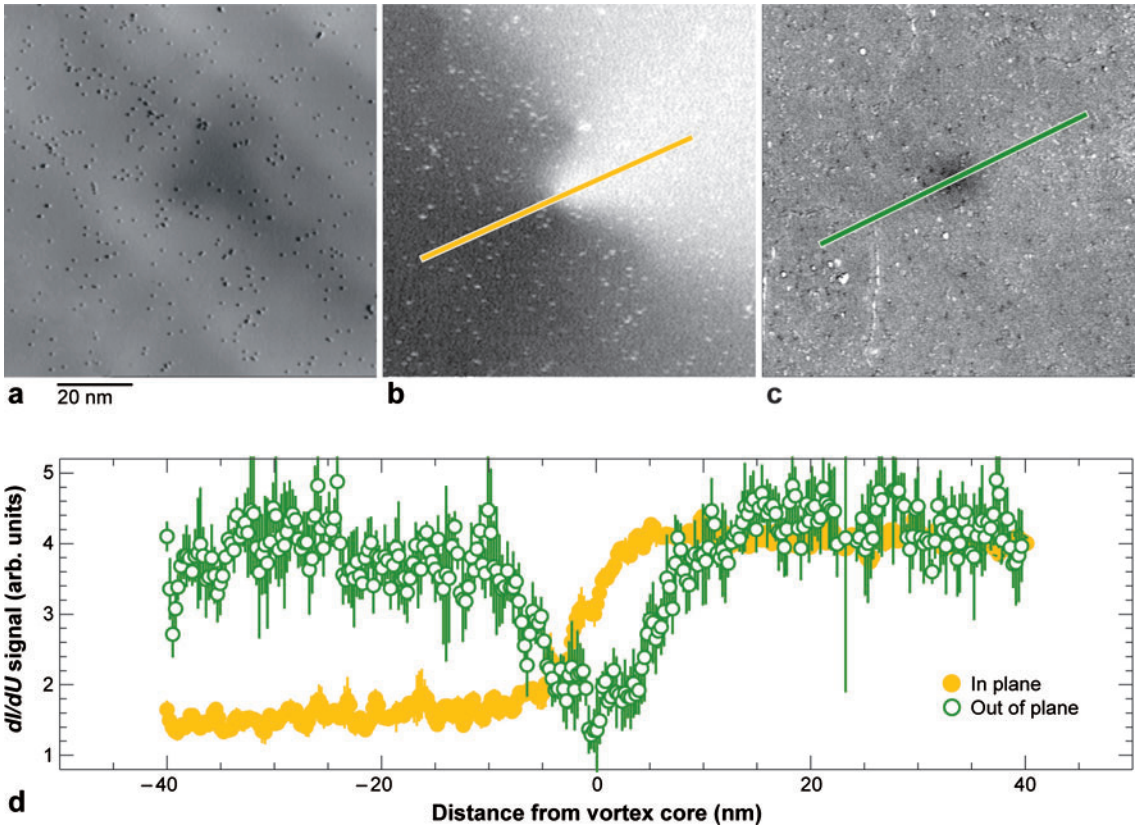

Figure 5

(*a*) Topography and (*b*) map of *dI/dU* of the same region of the vortex core in Fe on W(110) taken with an antiferromagnetic tip with in-plane sensitivity. (*c*) *dI/dU* map of the vortex core taken with an antiferromagnetic tip with out-of-plane sensitivity. (*d*) Line profile of the in-plane and out-of-plane component across the vortex core as indicated in *b* and *c*. The figure was kindly provided by M. Bode.

The experiments were done with a STM operating at 25 K in the spectroscopic mode. The magnetic Fe films were grown on clean W(001) substrates. Again, Fe-coated W tips were used to obtain in-plane spin contrast (26) in Sp-STM. In spite of the large misfit of 10.4%, Fe grows pseudomorphically on W(100) up to 4 ML coverage. At 500 K and for coverages above 5 ML, cross-shaped islands are nucleated on a 2 ML carpet of pseudomorphic Fe (see **Figure 6*d***). Magneto-optic Kerr effect (MOKE) measurements showed that films up to 4 ML are in-plane magnetized with a fourfold magnetic anisotropy with easy axis along ⟨110⟩.

As a first step toward Sp-STS, the local density of states of Fe structures was investigated. **Figure 6*a*** shows *dI/dU* spectra taken above 2, 3, and 4 ML films and cross-shaped islands (≈10 ML thick). We used specific electronic states to obtain magnetic contrast by means of Sp-STS, as displayed in the *dI/dU* spectra in **Figure 6*b***.

MOKE: magneto-optic Kerr effect

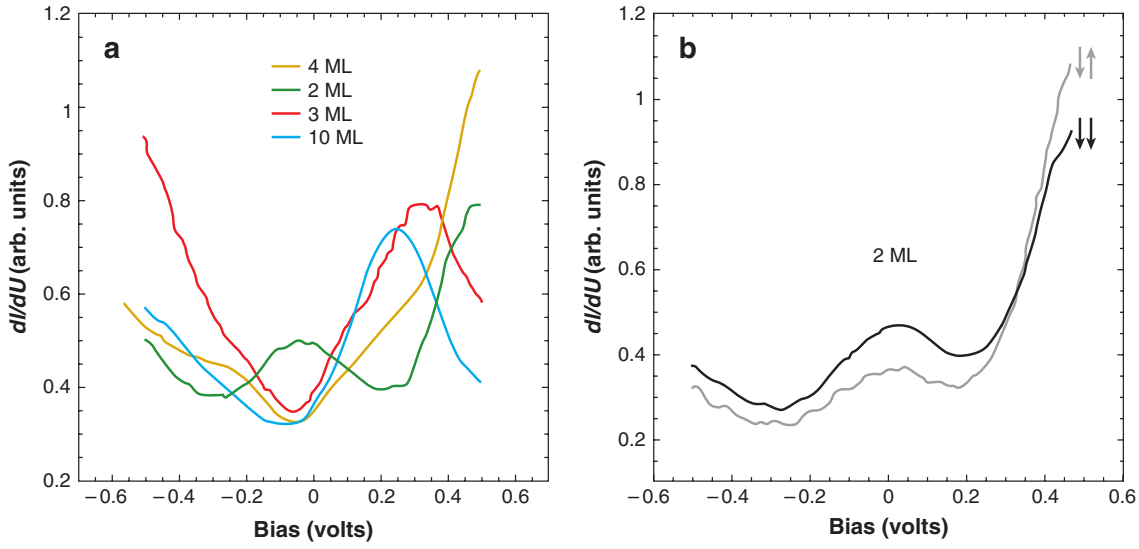

Figure 6

(*a*) *dI/dU* spectra taken above 2, 3, and 4 ML films and ≈10-ML-thick islands. (*b*) *dI/dU* spectra of two different magnetic domains on the 2 ML film. The peak at 0.25 V measured on thick islands corresponds to the well-known surface state of Fe(100). The spectra taken above the 3 ML and 4 ML islands show a peak and a shoulder at approximately 0.35 V. The spectrum taken above the 2 ML Fe film shows an occupied peak at approximately –0.1 V.

The spectra differ in peak height but not in peak position for parallel and antiparallel orientations of magnetization of tip and magnetic film.

Second, we focus on free domain walls in 2-ML-thick Fe films. The topographic image of a 2.3 ML Fe (see **Figure 7*a***) shows a continuous 2-ML-thick carpet of Fe and third ML islands as white dots. The *dI/dU* map of the same area (see **Figure 7*b***) shows contrasts of different origin. The thickness-related contrast between the 2 ML film and the 3-ML-high islands is due to the different electronic structure: The *dI/dU* at 0.3 V for the 3 ML areas is higher than that for 2 ML areas (see **Figure 7*a***). Additionally, **Figure 7*b*** shows two magnetic domains that are intermediate and dark. Typically, at least three contrast levels were resolved in agreement with the fourfold anisotropy. The rotation angle of the wall can be determined from the contrast change. **Figure 7*c*** shows a line profile taken across a 90° domain wall. A fit results in a wall width of $w = 12.4$ nm, a value that is five times lower than for bulk walls in Fe whiskers.

Whereas in bulk Fe Bloch walls are found, Néel walls are more favorable below a critical film thickness. In the limit of ultrathin films (thickness $d \ll w$), the Néel wall width w of a 90° wall is $w = \sqrt{A/K}$, with the exchange constant A and the anisotropy K (36). For a bulk 90° Bloch wall, the width is given by the same equation. This allows for a direct comparison of the microscopic parameters of bulk and ultrathin systems.

The reduced wall width in 2 ML Fe on W(100) as compared with bulk Fe is due to two reasons. First, the anisotropy in the thin film case is larger (for bulk Fe $K = 5.4 \times 10^4$ J m^{-3}, whereas we estimate $\approx -1.6 \times 10^5$ J m^{-3} from MOKE measurements of

Figure 7

(*a*) Topography and (*b*) map of *dI/dU* of the same region at 0.3 V of a 2.3 ML Fe grown on W(001) at 400 K (535 × 458 nm^2). (*c*) Line profile taken across a domain wall; the line profile is averaged over the white box in the inset. Circles represent experimental data, and the continuous line denotes the fit with a wall profile tanh(2*x*/*w*). (*d*) Topography and (*e*) map of *dI/dU* of 6 ML Fe grown on W(001) at 500 K (745 × 505 nm^2). (*f*) Line profile across the 90° domain wall within the white box pinned at the step edge.

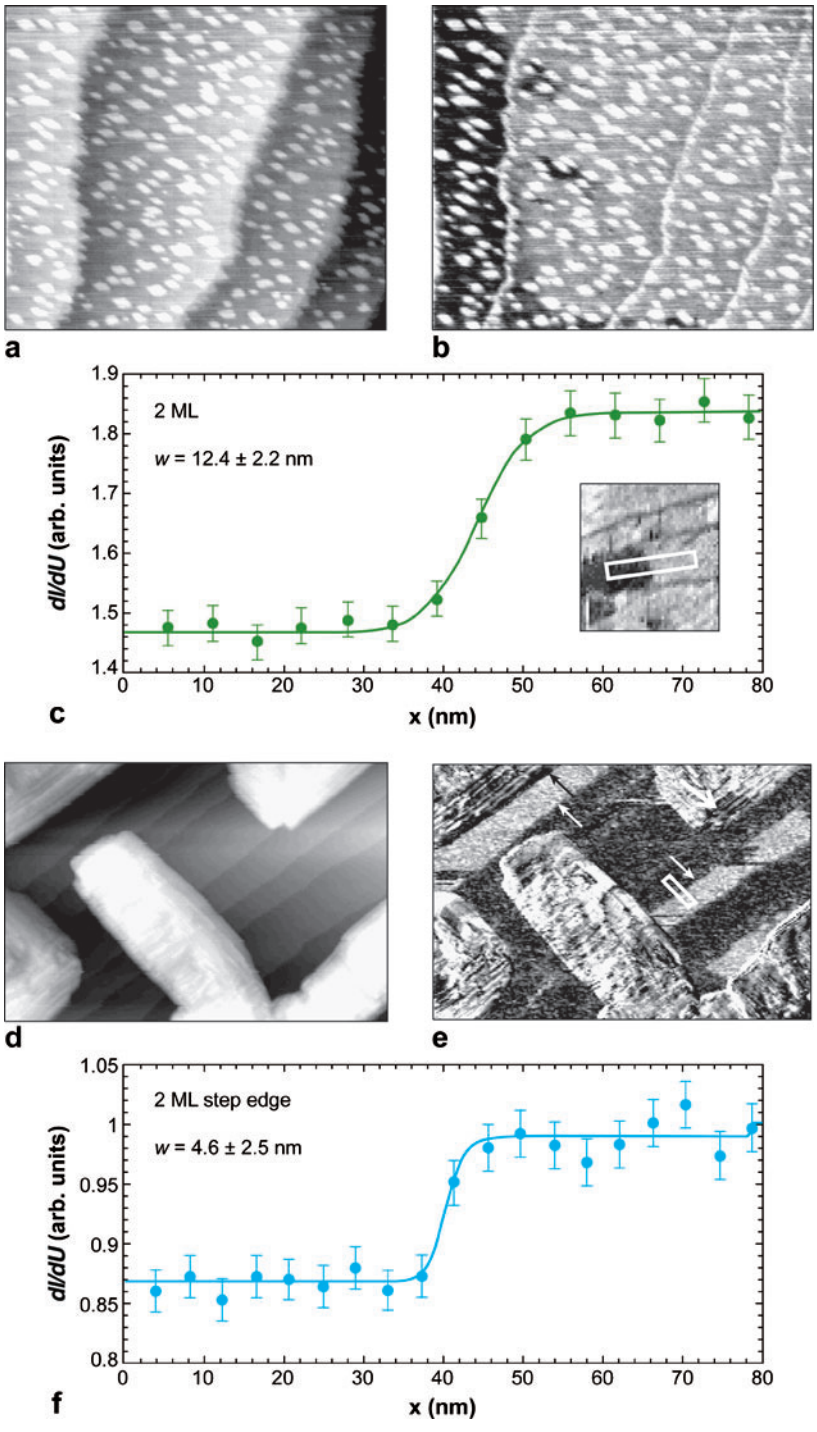

2 ML films). Second, the exchange constant A in 2 ML Fe is strongly reduced. The finite thickness of the film reduces the number of magnetic nearest neighbors by a factor of two as compared with bulk Fe, decreasing A. Both effects together explain the narrowing.

Finally, in some cases domain walls were pinned by W substrate step edges. **Figure 7*d*** shows an annealed film with islands. In between the islands, the substrate is covered by a continuous 2 ML Fe film. **Figure 7*e*** shows the local dI/dU signal of the same area. Again, the contrast in the dI/dU image between the islands and the 2 ML Fe film is due to the difference in their electronic structures. On the 2 ML film, several magnetic domains separated by 90° domain walls can be seen; some of the walls are pinned at the step edges, as indicated by the arrows in **Figure 7*e***. The line profile taken across the pinned domain wall (see **Figure 7*f***) indicates an even more reduced wall width of $w = 4.6$ nm. This further reduction can be explained by taking into account that the number of neighbors at the step edge of a 2 ML Fe film on W(100) is further reduced (37). Several next-nearest neighbors and nearest neighbors are missing at the step edge position. This reduces the exchange constant A. Additionally, the step edges induce a large magnetic anisotropy (38) localized at the step edge. Together both effects lead to the large observed decrease of the wall width. This also explains the pinning mechanism. If the wall is positioned above a step edge, the exchange energy is reduced.

Magnetic Configuration of Self-Organized Structures

Sp-STM in the spectroscopic contrast mode has been used in a variety of magnetic systems [Gd/W(110), Fe/W(110), Fe/W(100), Fe/Mo(110), and Co/Cu(111)] with ferromagnetic and antiferromagnetic tips that are sensitive to an in-plane or the out-of-plane component of the spin polarization (19, 20, 29, 37, 39–42). The direction of sensitivity depends on the magnetization direction of the last atom, which can be partly controlled using surface and interface magnetic anisotropies. Similarly, the differential magnetic mode has been used to map an in-plane or the out-of-plane component of the spin polarization in Fe, Ni, and Co (24, 43, 44). Out-of-plane contrast and in-plane contrast have been obtained with sharp, pointed tips and ring-shaped STM electrodes, respectively. Most studies have focused on the magnetic configuration of self-organized structures in the form of magnetic thin films or islands on nonmagnetic substrates. The domain structure within the islands and the relation of the magnetization of neighboring islands and stripes have been studied. The thermally activated switching of islands has been investigated, and the details of domain walls have been imaged. The field of nanomagnetism is capturing growing interest and currently expanding. More and more research groups have begun investigating magnetism, using Sp-STM.

ANTIFERROMAGNETIC FILMS

Antiferromagnets play an important role in pinning ferromagnets in spin-electronic devices such as hard-disk read heads, magnetic sensors, and future MRAM (7, 45).

Magnetic domain wall: the transition region between two domains

The spin structure of an antiferromagnetic surface is crucial for the exchange bias effect and is at the heart of understanding the coupling mechanism between the ferromagnet and antiferromagnet (46, 47).

Most antiferromagnetic materials are compounds in which the cations are separated by distances that are much larger than atomic distances in ferromagnetic materials. The exchange interaction occurs indirectly via nonmagnetic anions such as O^{2-}, e.g., MnO and NiO. Only a few metals—such as Cr, Mn, and some rare earth metals—possess antiferromagnetism. Their antiferromagnetic properties differ considerably from those observed for compounds because the antiferromagnetic coupling happens within neighboring atoms via direct exchange. Domains are present in both ferromagnetic and antiferromagnetic materials. Antiferromagnetic domains, however, have a different origin than those in ferromagnetic materials. Whereas in ferromagnetism the formation of domains can reduce the magnetostatic energy, in antiferromagnetism the presence of domains only increases the exchange energy because of additional disorder. Crystallographic defects may be needed to form antiferromagnetic domain walls.

Traditional methods to study antiferromagnets, such as neutron diffraction, are usually bulk sensitive and operate in reciprocal space. The development of Sp-STM made it possible to study (*a*) the spin configuration of antiferromagnetic surfaces on the atomic level (9) and (*b*) antiferromagnetic domains, domain walls, and nonperiodic features. Below we give several examples of collinear and noncollinear antiferromagnetic surface structures and illustrate the role of defects and frustrations.

Layer-Wise Antiferromagnets

A prototypic layer-wise antiferromagnet is body-centered cubic (bcc) Cr (48). Whereas Cr atoms within a (001) plane order ferromagnetically, neighboring (001) planes order antiferromagnetically. This was observed in early mixed topographic and spin images, using Sp-STM in the simple constant current mode (17). On this layer-wise antiferromagnetic order, an inconsumerate spin wave that leads to long-range variations of the Cr moment is superimposed.

Figure 8*a* shows a STM image of the topography of a clean Cr(001) surface consisting of atomically flat terraces separated by monoatomic step edges. According to the layer-wise antiferromagnetic order, neighboring terraces should have opposite spin polarization. Cr(001) displays a spin-polarized surface state near the Fermi edge (28), which can be used to obtain spin information in the spectroscopic mode of Sp-STM, employing an in-plane, magnetized, Fe-coated W tip. **Figure 8*b*** shows the *dI/dU* map of the same surface area. In the bottom part of the figure, the terraces show an alternating bright dark contrast, indicating the antiferromagnetic order. In addition, the central step disappears in the center of the image owing to a screw dislocation in the Cr crystal. This defect induces a frustration in the antiferromagnetic order, as there are three terraces in the top part and four terraces in the bottom part of the image. It is topologically impossible to keep an antiferromagnetic order of all terraces while keeping constant the spin polarization of each terrace. The solution to this topological problem is a frustration of the antiferromagnetic order by rotation

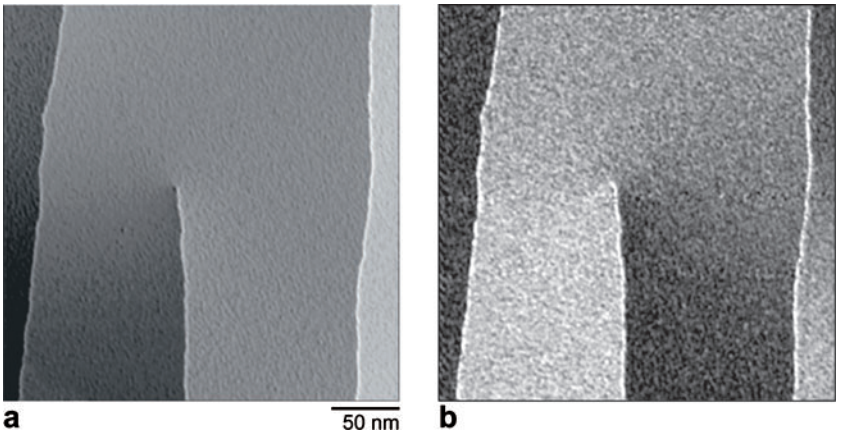

Figure 8

(*a*) Topography and (*b*) map of *dI/dU* of the same region near the Fermi edge of a Cr(001) surface. The images were taken with Fe-coated W tips. The figure is kindly provided by M. Bode.

of the spin polarization near the screw dislocation. This results in a gradual change of the spin signal from the top terrace around the dislocation to the lower terrace. Interestingly, the transition is smooth on length scales of 100 nm (49, 50). This is in contrast to the quite similar spin structure of the vortex cores in Fe, for which the smooth rotation is observed only very near to the vortex core. Several tens of nanometers away, the rotation of magnetization is split up into domains and domain walls owing to the interplay of magnetic anisotropy and exchange. The absence of domain wall formation in Cr hints at a low magnetic anisotropy. Similar studies on thin Cr films on Au(100) with screw dislocations revealed a much narrower transition of the spin polarization close to screw dislocations, indicating that anisotropy was higher in thin films than in bulk Cr (51).

Antiferromagnetic Domain Walls

In contrast to Cr, Mn shows a variety of modifications. The stable bulk phase of Mn at room temperature is α-Mn, which has a cubic structure containing 58 atoms per unit cell. Various other structural phases of Mn can be stabilized at room temperature by epitaxial growth on different substrates (52–54). Body-centered tetragonal (bct) Mn has been produced by epitaxial growth on Fe(001) with an in-plane lattice constant of Fe and an out-of-plane lattice constant that is 13% larger (55). The bct phase persists up to thicknesses between 10 ML and 20 ML, depending on the growth conditions (56). The bct Mn films show a layer-wise antiferromagnetic structure, as observed with Sp-STM in the spectroscopic mode through the use of Fe-coated W tips (21).

The simple, layer-wise antiferromagnetic order of Mn is pinned at the interface to Fe by the exchange interaction (56). This interaction, together with the antiferromagnetic order, leads to a frustration in the spin structure when atomic steps are present in Fe (cf. **Figure 9*a***). At the step edge of the substrate, Mn layers of opposite spin polarization meet. This leads to a magnetic frustration similar to a 180° domain wall in the Mn film. Owing to the vertical lattice mismatch (bcc Fe versus bct Mn), subatomic steps are formed at the Mn film surface at the position of Fe step edges. A region above

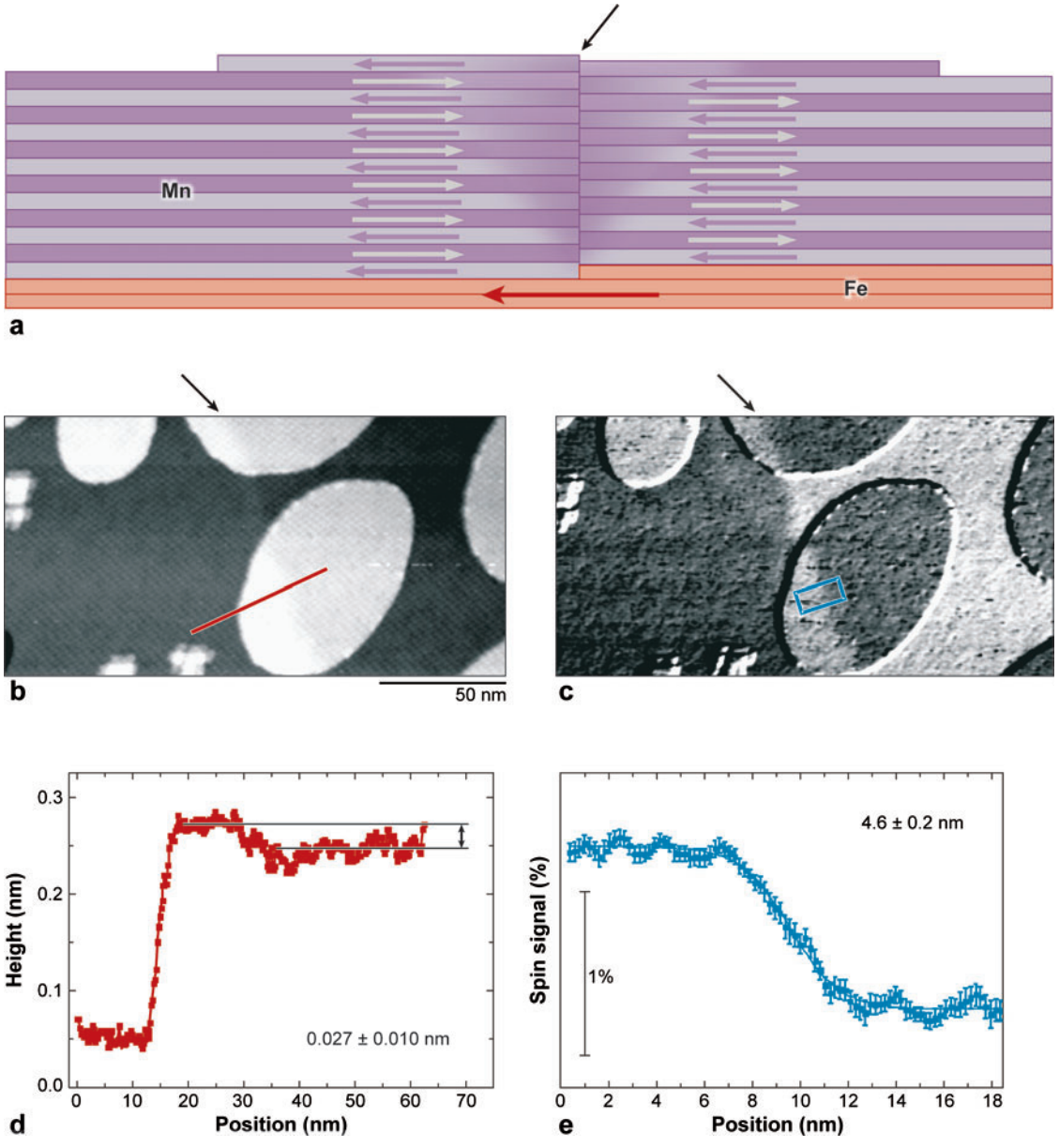

Figure 9

(*a*) Schematics of Mn overgrowing an Fe substrate step. The layer thickness of Mn is slightly larger than that of Fe, which causes a small step to appear (marked by a *black arrow*) in the topmost Mn layer. A magnetically frustrated region occurs above the buried Fe step edge. Sp-STM image of the (*b*) topography and (*c*) corresponding spin signal of 11.9 ML Mn on Fe(001). (*d*) Topographic line profile taken along the line in *b*. (*e*) Spin line profile across the frustrated region at the position of the box in *c*.

a buried Fe step edge is shown in **Figure 9*b*** for the topography and in **Figure 9*c*** for the corresponding spin signal measured in the differential magnetic mode via the use of a ring-shaped STM electrode. A buried Fe step edge is running almost vertically through the center of the image. The line profile in **Figure 9*d*** shows a step of monatomic height between two different Mn terraces (≈0.16 nm) and a step of subatomic height (≈0.018 nm) at the position of a buried Fe step edge. The latter is caused by the different lattice constants of Fe and Mn. In **Figure 9*c*** the layer-wise antiferromagnetic order between the Mn islands and the Mn layer underneath is clearly visible. Following the way of the buried Fe step edge, a magnetically frustrated region is found in the spin signal, where a reversal of contrast appears. **Figure 9*e*** presents an averaged line profile across the topologically enforced magnetic frustration at the position of the box in **Figure 9*c***. The measurements indicate that the magnetic frustration has a certain lateral extension. To estimate the wall width at the surface, the experimental profile is fitted with a $tanh(x/w)$ wall profile. The resulting width ($2w$) in this case was 4.6 ± 0.2 nm. A systematic study of the wall width as a function of the Mn film thickness has shown a linear widening of these regions with increasing Mn film thickness, which reflects an isotropic exchange interaction in the antiferromagnet (57).

A magnetic frustration in a layered antiferromagnet due to the exchange interaction with a ferromagnet is discussed above. The frustration is a topologically enforced domain wall, but the widths of the frustration are narrower than conventional domain walls in antiferromagnets. Domains walls in compensated antiferromagnets can also be present owing to a shift of the antiferromagnetic order by a primitive vector of the structural unit cell, as has been observed using Sp-STM on the c(2 × 2) antiferromagnetically ordered Fe ML on W(100) in the constant current mode (58).

Noncollinear Antiferromagnetism

The antiferromagnetic structures described above are all collinear systems; i.e., the magnetic moments of the atoms within the magnetic unit cell point in opposite

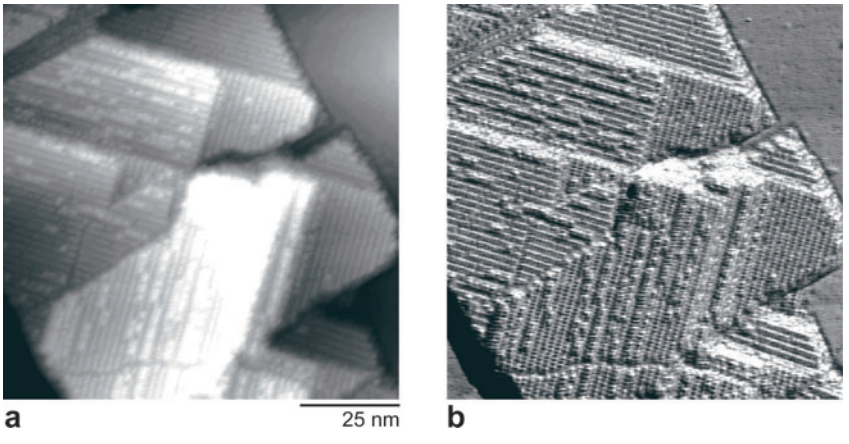

Figure 10

(*a*) Topography and (*b*) Sp-STM image of a reconstructed Mn film on Fe(001) recorded in the differential magnetic mode. The image sizes are 100 nm × 100 nm.

directions but along one axis. If more than two magnetic atoms are present in the unit cell, a second option exists: The total magnetic moment in the unit cell is compensated, but the individual magnetic moments lie on different axes. In this case, the spin configuration is noncollinear. A much larger variety of configurations is possible in this case such that in general these systems are much more complex than collinear spin structures. A fundamental problem arises when imaging noncollinear spin configurations with Sp-STM. The instrument is sensitive to only one component of the spin polarization. At least two components of the spin polarization are necessary to decide whether or not the structure is collinear.

In the case of Mn on Fe(001), the bct configuration is stable only up to ≈ 20 ML. Thicker films show a complex reconstruction. The reconstruction is accompanied by a roughening of the film, as shown in **Figure 10*a***. Islands several nanometers high are formed. On top of the islands, a fine reconstruction pattern with a unit cell of

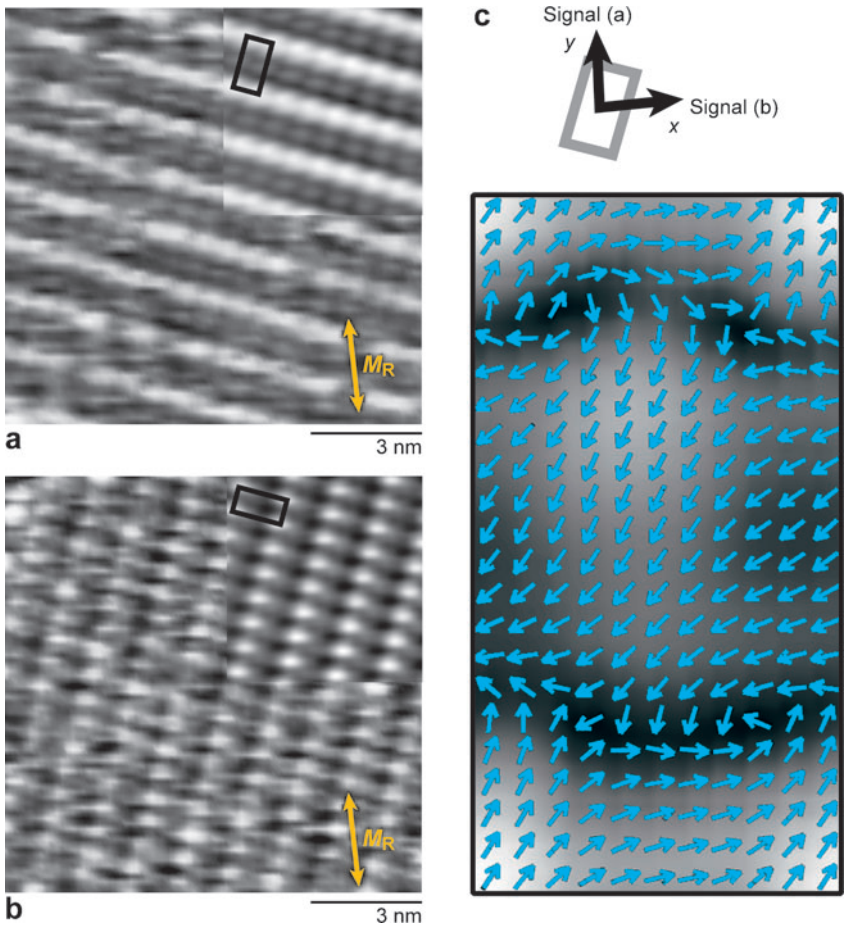

Figure 11

(*a*,*b*) Sp-STM images of two orthogonal reconstruction domains of Mn on Fe(001). The direction of sensitivity of the ring electrode is indicated. The insets show the same structure but as averaged over many unit cells to reduce the noise. (*c*) Vector map of the spin polarization within the unit cell combined from *a* and *b*. The *x* component of the spin polarization is given by the spin signal of *b* and the *y* component by the spin signal of *a*. The vectors (*blue arrows*) indicate the in-plane direction of the spin polarization, whereas the background gradient indicates the size of the spin polarization (black corresponds to zero, and white corresponds to the maximum).

$\approx 9 \times 18$ Å is found in the form of regular lines. Four equivalent domains exist on the surface owing to the fourfold symmetry of the Fe(001) substrate. The spin image recorded at the same time, using ring-shaped STM electrodes in the differential magnetic mode, shows a fine structure of the same unit cell on the islands (cf. **Figure 10*b***). As the ring magnetization lies tangential to the ring and in the ring plane, the direction of the in-plane sensitivity of the ring is well defined.

The Fe substrate can be rotated by 90°, and a second image of the spin structure of the four reconstruction domains can be taken. The spin structure observed with Sp-STM depends on only the relative orientation of the ring with respect to the reconstruction lines and is not related to the Fe orientation; i.e., the spin structure is determined only by the structure of the reconstruction. This allows one to combine data from two reconstruction domains of orthogonal line directions (see **Figure 11*a*,*b***) to build a vector map of the surface spin polarization, as depicted in **Figure 11*c***. The spin structure is noncollinear, as the vector directions show. Even the size of the in-plane spin polarization varies within the unit cell (**Figure 11*c***). The noncollinearity is also reflected by the different patterns of the two orthogonal measurements in **Figures 11*a*** and ***b***. For a collinear spin structure, the same pattern but of different intensities should be observed. Owing to the well-defined direction of sensitivity when ring-shaped STM electrodes are used, it is possible to detect noncollinear spin structures (59).

The surfaces of several antiferromagnetic films and crystals have been studied with Sp-STM. Besides the elementary antiferromagnets of Mn [on Fe(001) (21, 57) or W(110) (60)] and Cr [on Au(100) (51)], antiferromagnetic alloys such as NiMn and Mn_3N_2 (61) have also been studied. Additionally, antiferromagnetic Fe can be created as 1-ML-thick films on W(100) (8).

CONCLUSION

Sp-STM has evolved into a reliable and versatile tool for mapping atomic spin structures of ferromagnetic nanostructures and antiferromagnetic films with its different imaging modes. It can map the in-plane and out-of-plane components of spin polarization. Its superior lateral resolution and sensitivity have opened up a passway to study magnetism on its intrinsic scale. A fundamental problem, which is not solved with Sp-STM, is to relate the magnetic moment of an atom to its spin polarization. In the case of a constant electronic structure, however, magnetization and spin polarization are proportional. As a technique that focuses on electrons, Sp-STM is well equipped to address future issues related to modern spintronic devices.

ACKNOWLEDGMENTS

The authors acknowledge the many contributors to the presented work, especially Uta Schlickum, Chunlei Gao, Simona Bodea, and Atsushi Yamasaki. We also thank Matthias Bode for kindly contributing some of his data to this overview of this wide and quickly evolving field.

LITERATURE CITED

1. Zhu JG, Zheng Y, Prinz GA. 2000. Ultrahigh density vertical magnetoresistive random access memory. *J. Appl. Phys.* 87:6668–73
2. Stamm C, Marty F, Vaterlaus A, Weich V, Egger S, et al. 1998. Two-dimensional magnetic particles. *Science* 282:449–51
3. Kirk KJ, Chapman JN, Wilkinson CDW. 1997. Switching fields and magnetostatic interactions of thin film magnetic nanoelements. *Appl. Phys. Lett.* 71:539–41
4. Bussmann K, Prinz GA, Cheng SF, Wang D. 1999. Switching of vertical giant magnetoresistance devices by current through the device. *Appl. Phys. Lett.* 75:2476–78

5. Reports extremely large magnetic anisotropy of small atomic clusters.

5. **Gambardella P, Rusponi S, Veronese M, Dhesi SS, Grazioli C, et al. 2003. Giant magnetic anisotropy of single cobalt atoms and nanoparticles. *Science* 300:1130–33**
6. Rusponi S, Cren T, Weiss N, Epple M, Buluschek P, et al. 2003. The remarkable difference between surface and step atoms in the magnetic anisotropy of two-dimensional nanostructures. *Nat. Mater.* 2:546–51
7. Kuch W, Chelaru LI, Offi F, Wang J, Kotsugi M, Kirschner J. 2006. Tuning the magnetic coupling across ultrathin antiferromagnetic films by controlling atomic-scale roughness. *Nat. Mater.* 5:128–33

8. The first experimental imaging of antiferromagnetic Fe.

8. **Kubetzka A, Feriani P, Bode M, Heize S, Bilmayer G, et al. 2005. Revealing antiferromagnetic order of the Fe monolayer on W(001): spin-polarized scanning tunneling microscopy and first-principles calculation. *Phys. Rev. Lett.* 94:87204/1–4**

9. Provides a theoretical foundation for the interpretation of STM images.

9. **Tersoff J, Hamann DR. 1983. Theory and application for the scanning tunneling microscope. *Phys. Rev. Lett.* 50:1998–2001**
10. Tersoff J, Hamann DR. 1985. Theory of the scanning tunneling microscope. *Phys. Rev. B* 31:805–13

11. Announces the invention of STM.

11. **Binning G, Rohrer H, Gerber C, Weibel E. 1982. Tunneling through a controllable vacuum gap. *Appl. Phys. Lett.* 40:178–80**
12. Binning G, Rohrer H, Gerber C, Weibel E. 1982. Surface studies by scanning tunneling microscopy. *Phys. Rev. Lett.* 49:57–61

13. Reports the discovery of the TMR effect.

13. **Jullière M. 1975. Tunneling between ferromagnetic films. *Phys. Lett.* 54A:225–26**
14. Slonczewski JC. 1989. Conductance and exchange coupling of two ferromagnets separated by a tunneling barrier. *Phys. Rev. B* 39:6995–7002
15. Miyazaki T, Tezuka N. 1995. Giant magnetic tunneling effect in Fe/Al_2O_3/Fe junction. *J. Magn. Magn. Mater.* 139:L231–34

16. Proposed the four fundamental imaging modes of Sp-STM.

16. **Pierce DT. 1988. Spin-polarized electron microscopy. *Phys. Scr.* 38:291–96**

17. The first Sp-STM results in the constant current mode.

17. **Wiesendanger R, Güntherodt HJ, Güntherodt G, Gambino RJ, Ruf R. 1990. Observation of vacuum tunneling of spin-polarized electrons with the scanning tunneling microscope. *Phys. Rev. Lett.* 65:247–50**

18. The first Sp-STM results with optically pumped GaAs tips.

18. **Suzuki Y, Nabhan W, Tanaka K. 1997. Magnetic domains of cobalt ultrathin films observed with a scanning tunneling microscope using optically pumped GaAs tips. *Appl. Phys. Lett.* 71:3153–55**

19. Bode M, Getzlaff M, Wiesendanger R. 1998. Spin-polarized vacuum tunneling into the exchange-split surface state of Gd(0001). *Phys. Rev. Lett.* 81:4256–59

20. Kubetzka A, Bode M, Pietzsch O, Wiesendanger R. 2002. Spin-polarized scanning tunneling microscopy with antiferromagnetic probe tips. *Phys. Rev. Lett.* 88:057201/1–4

21. Yamada TK, Bischoff MMJ, Heijnen GMM, Mizoguchi T, van Kempen H. 2003. Observation of spin-polarized surface states on ultrathin bct Mn(001) films by spin-polarized scanning tunneling spectroscopy. *Phys. Rev. Lett.* 90:056803/1–4

22. Wulfhekel W, Kirschner J. 1999. Spin-polarized scanning tunneling microscopy on ferromagnets. *Appl. Phys. Lett.* 75:1944–46

23. Johnson M, Clarke J. 1990. Spin-polarized scanning tunneling microscope: concept, design, and preliminary results from a prototype operated in air. *J. Appl. Phys.* 67:6141–52

24. Schlickum U, Wulfhekel W, Kirschner J. 2003. Spin-polarized scanning tunneling microscope for imaging the in-plane magnetization. *Appl. Phys. Lett.* 83:2016–18

25. Ha JK, Hertel R, Kirschner J. 2002. Thickness dependence of magnetization structures in thin permalloy rectangles. *Z. Metallkd.* 93:957–62

26. Pratzer M, Elmer HJ, Bode M, Pietzsch O, Kubetzka A, Wiesendanger R. 2001. Atomic-scale magnetic domain walls in quasi-one-dimensional Fe nanostripes. *Phys. Rev. Lett.* 87:127201/1–4

27. Wulfhekel W, Zavaliche F, Hertel R, Bodea S, Steierl G, et al. 2003. Growth and magnetism of Fe nanostructures on W(001). *Phys. Rev. B* 68:144416/1–9

28. Stroscio JA, Pierce DT, Davies A, Celotta JR. 1995. Tunneling spectroscopy of bcc (001) surface states. *Phys. Rev. Lett.* 75:2960–63

29. Yamasaki A, Wulfhekel W, Hertel R, Suga S, Kirschner J. 2003. Direct observation of the single-domain limit of Fe nanomagnets by spin-polarized scanning tunneling spectroscopy. *Phys. Rev. Lett.* 91:127202/1–4

30. Cowburn RP, Koltsov DK, Adeyeye AO, Welland ME, Tricker DM. 1999. Single domain circular nanomagnets. *Phys. Rev. Lett.* 83:1042–45

31. Shinjo T, Okuno T, Hassdorf R, Shigeto K, Ono T. 2000. Magnetic vortex core observation in circular dots of permalloy. *Science* 289:930–32

32. Feldtkeller E, Thomas H. 1965. Struktur und Energie von Blochlinien in dünnen ferromagnetischen Schichten. *Phys. Kondens. Mater.* 4:8–14

33. Wachowiak A, Wiebe J, Bode M, Pietzsch O, Morgenstern M, Wiesendanger R. 2002. Direct observation of internal spin structure of magnetic vortex cores. *Science* 298:577–80

34. Haibach P, Huth M, Adrian H. 2000. Step-edge induced anisotropic domain-wall propagation. *Phys. Rev. Lett.* 84:1312–15

35. Bruno P. 1999. Geometrically constrained magnetic wall. *Phys. Rev. Lett.* 83:2425–28

36. Middelhoek S. 1963. Domain walls in thin NiFe films. *J. Appl. Phys.* 34:1054–59

37. Bodea S, Wulfhekel W, Kirschner J. 2005. The influence of step edges and strain on the domain wall widths. *Phys. Rev. B* 72:100403R/1–4

19. The first Sp-STM results in the spectroscopic mode.

22. The first Sp-STM results in the differential magnetic mode.

29. The first direct observation of the single-domain limit.

33. The first fully resolved images of the core of a magnetic vortex.

38. Chen J, Erskine JL. 1992. Surface-step-induced magnetic anisotropy in thin epitaxial Fe films on W(001). *Phys. Rev. Lett*. 68:1212–15
39. Pietzsch O, Kubetzka A, Bode M, Wiesendanger R. 2000. Real-space observation of dipolar antiferromagnetism in magnetic nanowires by spin-polarized scanning tunneling spectroscopy. *Phys. Rev. Lett*. 84:5212–15
40. Bode M, Pietzsch O, Kubetzka A, Wiesendanger R. 2004. Shape-dependent thermal switching behavior of superparamagnetic nanoislands. *Phys. Rev. Lett*. 92:067201/1–4
41. Pietzsch O, Kubetzka A, Bode M, Wiesendanger R. 2004. Spin-polarized scanning tunneling spectroscopy of nanoscale cobalt islands on Cu(111). *Phys. Rev. Lett*. 92:057202/1–4
42. Prokop J, Kukunin A, Elmers HJ. 2005. Magnetic anisotropies and coupling mechanisms in Fe/Mo(110) nanostripes. *Phys. Rev. Lett*. 95:187202-1-4
43. Ding HF, Wulfhekel W, Kirschner J. 2002. Ultra sharp domain walls in the closure domain pattern of Co(0001). *Eur. Phys. Lett*. 57:100–6
44. Wulfhekel W, Ding HF, Lutzke W, Steierl G, Vazquez M, et al. 2001. High resolution magnetic imaging by local tunneling magnetoresistance. *Appl. Phys. A* 72:463–70
45. Nakamura K, Freeman AJ, Wang DS, Zhong L, Fernandez-de-Castro J. 2001. Magnetic structures at the ferromagnetic NiFe and antiferromagnetic NiMn interface in exchange-biased films: role of noncollinear magnetism and roughness. *Phys. Rev. B* 65:012402/1–4
46. Malozemoff AP. 1987. Random-field model of exchange anisotropy at rough ferromagnetic-antiferromagnetic interfaces. *Phys. Rev. B* 35:3679–82
47. Stamps RL. 2000. Mechanisms for exchange bias. *J. Phys. D* 33:R247–48
48. Blügel S, Pescia D, Dederichs PH. 1989. Ferromagnetism versus antiferromagnetism of the Cr(001) surface. *Phys. Rev. B* 39:1392–94
49. Kleiber M, Bode M, Ravlic R, Wiesendanger R. 2000. Topology-induced spin frustrations at the Cr(001) surface studied by spin-polarized scanning tunneling spectroscopy. *Phys. Rev. Lett*. 85:4606–9
50. Ravlic R, Bode M, Kubetzka A, Wiesendanger R. 2003. Correlation of dislocation and domain structure of Cr(001) investigated by spin-polarized scanning tunneling microscopy. *Phys. Rev. B* 67:174411/1–11
51. Kawagoe T, Iguchi Y, Miyamachi T, Yamasaki A, Suga S. 2005. Spiral terraces and spin frustration in layered antiferromagnetic Cr(001) films. *Phys. Rev. Lett*. 95:207205/1–4
52. Arrott AS, Heinrich B, Purcell ST, Cochran JF, Urquhart KB. 1987. Engineering magnetic materials on the atomic scale. *J. Appl. Phys*. 61:3721–28
53. Wuttig M, Gauthier Y, Blüugel S. 1993. Magnetically driven buckling and stability of ordered surface alloys: Cu(100) c(2 2)Mn. *Phys. Rev. Lett*. 70:3619–22
54. Rader O. 1997. Electronic structure of two-dimensional magnetic alloys: c(2 2) Mn on Cu(100) and Ni(100). *Phys. Rev. B* 55:5404–15
55. Kim SK, Tian Y, Montesano M, Jona F, Marcus PM. 1996. Simple structure and soft elastic behavior of Mn on Fe(001). *Phys. Rev. B* 54:5081–85

46. Provides a theoretical explanation of the size of the exchange bias effect.

56. Tulchinsky D, Unguris J, Celotta R. 2000. Growth and magnetic oscillatory exchange coupling of Mn/Fe(001) and Fe/Mn/Fe(001). *J. Magn. Magn. Mater.* 212:91–100
57. Schlickum U, Janke-Gilman N, Wulfhekel W, Kirschner J. 2004. Step-induced frustration of antiferromagnetic order in Mn on Fe(001). *Phys. Rev. Lett.* 92:107203/1–4
58. Bode M, Vedmedenko Y, von Bergmann K, Kubetzka A, Ferriani P, et al. 2006. Atomic spin structure of antiferromagnetic domain walls. *Nat. Mater.* 5:477–81
59. Gao CL, Schlickum U, Wulfhekel W, Kirschner J. 2007. Mapping the surface spin structure of large unit cells: reconstructed Mn films on Fe(001). *Phys. Rev. Lett.* 98:107203
60. Heinze S, Bode M, Kubetzka A, Pietzsch O, Nie X, et al. 2002. Real-space imaging of two-dimensional antiferromagnetism on the atomic scale. *Science* 288:1805–8
61. Yang H, Smith AR, Prikhodko M, Lambrecht WRL. 2002. Atomic-scale spin-polarized scanning tunneling microscopy applied to Mn_3N_2 (010). *Phys. Rev. Lett.* 89:226101/1–4

Annual Review of
Materials Research

Volume 37, 2007

Contents

MATERIALS CHARACTERIZATION